USGS
science for a changing world

Shallow-Depth Location and Geometry of the Piedmont Reverse Splay of the Hayward Fault, Oakland, California

Open-File Report 2016–1123

U.S. Department of the Interior
U.S. Geological Survey

Cover: Photograph of the area of the near-surface trace of the Piedmont Reverse splay and the setup site for the multi-channel array used to acquire the seismic data discussed in this report.

Shallow-Depth Location and Geometry of the Piedmont Reverse Splay of the Hayward Fault, Oakland, California

By Rufus D. Catchings, Mark R. Goldman, David Trench, Michael Buga, Joanne H. Chan, Coyn J. Criley, and Luther M. Strayer

Open-File Report 2016–1123

U.S. Department of the Interior
U.S. Geological Survey

U.S. Department of the Interior
RYAN K. ZINKE, Secretary

U.S. Geological Survey
William H. Werkheiser, Acting Director

U.S. Geological Survey, Reston, Virginia: 2017

Suggested citation:
Catchings, R.D., Goldman, M.R., Trench, David, Buga, Michael, Chan, J.H., Criley, C.J., and Strayer, L.M., 2017, Shallow-depth location and geometry of the Piedmont Reverse splay of the Hayward Fault, Oakland, California: U.S. Geological Survey Open-File Report 2016–1123, 22 p., https://dx.doi.org/10.3133/ofr20161123.

ISSN 2331-1258 (online)

Contents

Figures

Shallow-Depth Location and Geometry of the Piedmont Reverse Splay of the Hayward Fault, Oakland, California

By Rufus D. Catchings,[1] Mark R. Goldman,[1] David Trench,[2] Michael Buga,[3] Joanne H. Chan,[1] Coyn J. Criley,[1] and Luther M. Strayer[4]

Introduction

The Piedmont Thrust Fault, herein referred to as the Piedmont Reverse Fault (PRF), is a splay of the Hayward Fault that trends through a highly populated area of the City of Oakland, California (fig. 1*A*). Although the PRF is unlikely to generate a large-magnitude earthquake, slip on the PRF or high-amplitude seismic energy traveling along the PRF may cause considerable damage during a large earthquake on the Hayward Fault. Thus, it is important to determine the exact location, geometry (particularly dip), and lateral extent of the PRF within the densely populated Oakland area. In the near surface, the PRF juxtaposes Late Cretaceous sandstone (of the Franciscan Complex Novato Quarry terrane of Blake and others, 1984) and an older Pleistocene alluvial fan unit along much of its mapped length (fig. 1*B*; Graymer and others, 1995). The strata of the Novato Quarry unit vary greatly in strike (NW, NE, and E), dip direction (NE, SW, E, and NW), dip angle (15° to 85°), and lithology (shale and sandstone), and the unit has been intruded by quartz diorite in places. Thus, it is difficult to infer the structure of the fault, particularly at depth, with conventional seismic reflection imaging methods. To better determine the location and shallow-depth geometry of the PRF, we used high-resolution seismic imaging methods described by Catchings and others (2014). These methods involve the use of coincident P-wave (compressional wave) and S-wave (shear wave) refraction tomography and reflection data, from which tomographic models of P- and S-wave velocity and P-wave reflection images are developed. In addition, the coincident P-wave velocity (V_P) and S-wave velocity (V_S) data are used to develop tomographic models of V_P/V_S ratios and Poisson's ratio, which are sensitive to shallow-depth faulting and groundwater. In this study, we also compare measurements of S-wave velocities determined from surface waves with those determined from refraction tomography. We use the combination of seismic methods to infer the fault location, dip, and the National Earthquake Hazards Reduction Program (NEHRP) site classification along the seismic profile. Our seismic study is a smaller part of a larger study of the PRF by Trench and others (2016).

[1]U.S. Geological Survey
[2]InfraTerra, Inc.
[3]Fugro Consultants, Inc.
[4]California State University, East Bay

Seismic Data Acquisition

In February 2015, we acquired high-resolution P- and S-wave seismic data along a two-dimensional (2D) profile across the mapped trace of the PRF at Dimond Park in Oakland (fig. 1*C*). Our seismic profile was 315 m long and trended southwest to northeast. We acquired the P- and S-wave data separately using hammer sources (shots) consisting of vertical (for P-waves) and horizontal (for S-waves) hammer blows on aluminum blocks. Each shot was co-located with a geophone, and all P- and S-wave shots were recorded by 106 P-wave (40-Hz) and 106 S-wave (4.5-Hz) geophones, respectively. The spacing between geophones was 3 m. All data were recorded using two Geometrics RX-60 multi-channel seismograph systems (each with 60 channels) that were connected to refraction cables.

We recorded the data in two phases. First, we deployed vertical-component sensors along the seismic profile and used vertical hammer blows (P-wave shots) at each sensor to record P-wave data along the entire array, thereby using a total of 106 shot points, each recorded by 106 sensors, for the P-wave dataset. We then substituted the horizontal-component sensors for the vertical-component sensors and used horizontal hammer blows (S-wave shots) on a weighted aluminum block at the same shot points, thereby using a total of 106 shot points, each recorded by 106 sensors, for the S-wave dataset.

Seismic Data

By using 106 shots per dataset that were each recorded by 106 sensors, the P- and S-wave datasets consisted of approximately 11,236 traces each along the 315-m-long seismic profile. The density of the data allows for the high redundancy needed for both tomographic modeling and reflection stacking. Because the P-wave data were recorded with vertical-component geophones, the data consist dominantly of compressional (P) body waves and associated surface (Raleigh) waves (fig. 2*A*, *B*). Similarly, the S-wave data were recorded with horizontal-component geophones, which yield data that dominantly consist of Love waves (fig. 2*C*, *D*).

Seismic Data Processing

The acquisition geometry allowed us to develop multiple types of seismic models and images, including (1) P-wave refraction tomography, (2) P-wave reflection images, (3) S-wave refraction tomography, (4) a V_P/V_S ratio model, and (5) a Poisson's ratio model. We also had the option of developing S-wave reflection images, but as we discuss below, reflection imaging is not an ideal method for seismic imaging because of the complex geology; thus, we concentrated on tomography imaging. Our refraction tomography models were developed using the code of Hole (1992), and the reflection data were processed using ProMax, an interactive data processing package.

In addition to refraction tomography and reflection data processing, the acquisition geometries also allow us to develop Raleigh- and Love-wave velocity models using the Multi-channel Analysis of Surface Waves (MASW) method, first developed by Park and others (1999). For inversion of the Dimond Park dataset, we used the modified MASW method of Hayashi and Suzuki (2004) and Hayashi (2008). We analyzed Raleigh waves from the P-wave dataset and Love waves from the S-wave dataset using the MASW method. We refer to the S-wave velocity model developed from Raleigh waves as the MASW velocity model and the model developed from Love waves as the Multi-channel Analysis of Love Waves (MALW) model.

P-Wave Refraction Tomography Velocity Model

We developed a P-wave refraction tomography velocity model from first-arrivals measured on P-wave shot gathers using the algorithm of Hole (1992). We inverted the velocity model using a 3-m by 3-m grid and as many as 11,236 first-arrivals, which allowed for a high degree of redundancy and resolution within the model. Our starting models were developed from one-dimensional (1D) analysis of shot gathers along the profile. We used multiple starting models, but all final models were similar, with less than about 2 percent variation among the models where best resolved. Our preferred final model is shown in figure 3. The P-wave velocities range from about 600 to 2,100 meters per second (m/s) on the southwestern side of the profile, but P-wave velocities are considerably higher on the northeast side, ranging from about 800 to 3,200 m/s. There is a clear, near-vertical discontinuity in velocities from the northeast to the southwest between meters 150 and 175 of the seismic profile, where there is also a prominent topographic peak at the surface. In this report, we interpret this prominent, near-vertical velocity discontinuity, which coincides with other seismic anomalies discussed below, to be a major trace of the PRF in the upper 50 m. At depths below about 50 m, higher P-wave velocities extend southwest of the 150- to 175-m range. However, we suggest that the higher P-wave velocities below that depth (southwest of the fault) likely arise from the top of the same rocks seen on the northeastern side of the fault. There is also a down-to-the-southwest offset in the 1,500 m/s velocity contour, which has been shown to coincide with the top of static groundwater in numerous studies (see Catchings and others, 2014, for a summary), across our interpreted fault. The offset in the inferred depth to the top of groundwater suggests that this trace of the PRF is a groundwater barrier.

S-Wave Refraction Tomography Velocity Model

We developed an S-wave refraction tomography velocity model from first-arrivals measured on the S-wave shot gathers, also using the algorithm of Hole (1992). As with the P-wave model, we used a 3-m by 3-m grid and a large number of the 11,236 S-wave first-arrivals that were available, which similarly allows for a high degree of redundancy and resolution for the S-wave model. Because first-arrivals for the longer offset traces were contaminated with cultural (dominantly traffic) noises, we opted not to use a number of the longer offset arrivals. This resulted in a shallower depth of S-wave imaging than with the P-wave arrivals.

For S-wave modeling, we also used multiple 1D starting velocity models as input to the tomographic inversion. However, each starting model yielded a similar final model, suggesting that the model is well resolved. Our preferred 2D S-wave model is shown in figure 4. S-wave velocities range from about 260 to 520 m/s on the southwest side of the profile to about 500 to 800 m/s on the northeast side. As with the P-wave velocity model, there is a sharp transition from the higher S-wave velocities on the northeast to the lower S-wave velocities on the southwest along a near-vertical discontinuity centered near meter 160, beneath a prominent topographic peak. Because of the sensitivity of S-waves to the rigidity of lithologic units, we suggest that the tomographic S-wave velocity model best illustrates the faulted discontinuity between the sandstone (of the Novato Quarry terrane of Blake and others, 1984) and the older Pleistocene alluvial unit. This suggests that this trace of the PRF is dominantly near vertical (~80–85°) in the upper few tens of meters at Dimond Park, and it is centered between meters 150 and 160 near the surface along our seismic profile.

V_P/V_S Model

Using the method described by Catchings and others (2014), we developed models of V_P/V_S ratios along the seismic profile (fig. 5). Because we used the same model parameters and profile geometry for the P- and S-wave velocity models, V_P/V_S models along the profile could be developed by dividing the P-wave velocity by the S-wave velocity at each node of the velocity models. However, because the maximum depth of tomography imaging was shallower for the S-wave model than the P-wave model, we could develop the V_P/V_S ratio model only to the maximum depth of the S-wave model.

V_P/V_S ratios range from about 1.6 to 4.2, with the lowest ratios in the near-surface at the topographic high near the center of the seismic profile and the highest values to the southwest and northeast ends of the profile. An area of prominent low V_P/V_S ratios near meter 150 (beneath the topographic high) is observed at 10–50 m below the surface. This low value is oriented near vertically, with a slight northeasterly dip (~79°). We suggest that the V_P/V_S model is more sensitive to the fault structure at depths greater than about 20 m than either of the refraction tomography models. Thus, the dip of the fault, as inferred from the V_P/V_S model, is likely about 80° toward the northeast.

Poisson's Ratio Model

In a manner similar to that for V_P/V_S ratios, we used the P- and S-wave velocity models to develop a model of Poisson's ratio ($V_P^2 - 2V_S^2 / 2(V_P^2 - V_S^2)$) along the seismic profile (fig. 6). Poisson's ratio varies from about 0.2 near the surface beneath the central topographic high to about 0.47 near the southwest and northeast ends of the profile at about 20–40 m below the surface. Poisson's ratio for materials can vary widely, but the maximum value of 0.5 typically correlates with a fluid. There is an area of relatively low Poisson's ratios directly beneath the topographic high, near the center of the seismic profile. Because shallow-depth Poisson's ratios of about 0.43 have been shown to correlate with highly water-saturated materials (Catchings and others, 2014), our model suggests the fault along the central part of our seismic profile (fault zone) is water saturated only at depths greater than about 40 m, but areas to the southwest and northeast are water saturated at relatively shallow depths (as shallow as 3 m on the SW and 8 m on the NE). The shallow, highly saturated zones inferred from Poisson's ratio differ from the top of groundwater inferred above from the V_P = 1,500 m/s contour (which does not show the prominent low at the fault zone) because the lower resolution of the P-waves may not image relatively narrow zones of low velocities (such as faults) at depths of several tens of meters. The relatively shallow zones of high saturation (high Poisson's ratio) likely arise from watering of the grass in Dimond Park, particularly to the southwest, but those shallow zones probably do not reflect the depth to the static groundwater level. The relatively low Poisson's ratio values at the fault further suggest that the fault acts as a barrier to groundwater flow.

Seismic Reflection Images

We developed a seismic reflection stack of the data using the P-wave data from our seismic survey (fig. 7*A*). Semi-continuous reflections are observed along the southwestern part of our seismic profile (between distance meters 0 and 75, within the upper 50 m of depth), which consists of older Pleistocene alluvium, but continuous reflections are largely absent along the northeastern part of our seismic profile (meters 140 to ~300), which consists of the dominantly

disrupted and variably dipping sandstone. This variation in reflectivity suggests that the rocks beneath the northeastern part of the seismic profile are not well layered or are not continuously sub-horizontally layered, which is consistent with geologic mapping in the area. According to Graymer and others (1995), the dip of the sandstone unit in our immediate study area varies from about 57° southwest to about 50° northeast, and within hundreds of meters of our seismic line dips vary even more widely, from about 80° southwest to 65° northeast (fig. 1*B*). In addition, northwest and easterly dips are also observed and range up to 85°. Thus, we would not expect highly resolved reflection images along our seismic profile.

We do, however, observe reflection evidence for structures that are consistent with the mapped geology in the area. Near the southwestern end of the profile, the surface geology consists of Holocene fan and fluvial deposits, which presumably overlie Pleistocene alluvial fan and fluvial deposits. There is little topography associated with these deposits along the southwestern end of the seismic profile, suggesting that they should be dominantly sub-horizontally layered deposits. On the southwestern end of the seismic reflection image, we observe sub-horizontal reflectors in the upper 40–50 m, underlain by northeasterly to sub-horizontally dipping reflectors (fig. 7*A*).

Near the center of the seismic profile (~meter 158), geologic mapping (fig. 1*B*) suggests northeastward dipping (~50°) strata, and we similarly observe northeasterly dipping reflections on our seismic image. North of the northern end of our seismic profile, geologic mapping (fig. 1*B*) suggests southwest-dipping (~57°) strata, and we similarly observe southwesterly dipping strata on the seismic reflection image. The large variations in strike, dip, and lithology, however, suggest that laterally continuous reflections are unlikely to be observed along the length of our seismic profile. In addition, there are prominent diffractions in places along the seismic profile, particularly near the central part of the seismic profile (meters 150–160) and several locations (meters 200–250 and near meter 300) to the northwest (fig. 7*A*). These diffractions further distort the reflection image. Such diffractions, which can be seen to at least 300-m depth, typically coincide with disruptions in rock strata, such as offsets caused by faulting or intrusions. To better understand the cause of the diffractions observed along our seismic profile, we superimposed our S-wave tomography image on our reflection image to better interpret the reflection image (fig. 7*B*). We compare the S-wave tomography image because S-wave velocities are more sensitive to the rock type (rigidity), unlike the P-wave velocities, which are more sensitive to groundwater. The combined S-wave velocity and reflection image shows that diffractions correlate with the major lateral change in velocity between meters 150 and 160 of the seismic profile, further suggesting that the this trace of the PRF is located in the 150–160 m distance range of our seismic profile.

MASW and MALW S-Wave Velocity Models

We also developed 2D S-wave velocity models of the shallow subsurface using the MASW method of Hayashi (2008). We used both Raleigh waves from the P-wave data (fig. 8) and Love waves from the S-wave data (fig. 9) to compare the velocity structure inferred by the two surface-wave methods with that inferred from the S-wave tomography image (fig. 4). Whereas the two MASW models are different in detail, both show a prominent decrease in velocity from the northeast to the southwest ends of the profile, with the major change in velocity near the center of the seismic profile. On the southwest end of the seismic profile, S-wave velocities range from about 240 m/s to about 500 m/s, and on the northeast end of the seismic profile, S-wave velocities range from about 500 m/s to about 800 m/s. The maximum

change in velocity (as shown by the density of velocity contours) is slightly northeast of the topographic high along a series of near-vertical contours. The MASW and MALW 2D S-wave models, which essentially consist of a series of 1D models, are laterally less accurate than the tomographic S-wave model, but both surface-wave-based S-wave models show similar velocities, a strong lateral variation in velocity, and near-vertical velocity contours near the fault zone (meters 150–200).

Surface-wave methods, such as MASW, are widely used to evaluate S-wave velocities for site classification purposes; however, the comparisons shown here demonstrate that the surface-wave methods are generally less accurate than tomography methods in determining S-wave velocities for any given locality, especially when there are strong lateral variations in velocity and topography.

Summary and Seismic Interpretation

All seismic velocity models (both P- and S-wave) show a near-vertical prominent change in velocity between meters 150 and 160 of the Dimond Park seismic profile. Lower seismic velocities are observed to the southwest and substantially higher velocities are observed to the northeast. Two-dimensional MASW and MALW S-wave velocity images show similar lateral changes in velocity (fig. 8, 9), but the lateral transition in velocities is less abrupt, owing to the inherently lower resolution of the surface-wave methods. V_P/V_S and Poisson's ratios are higher to the northeast and southwest of meters 150–160, with prominent low-ratio values directly beneath this zone (figs. 5, 6). A reflection stack shows that the zone near meters 150–160 of our seismic profile includes prominent diffractions from the near surface to at least 300-m depth (fig. 7). The laterally varying and high-angle dips of strata (up to 80° northeast to 80° southwest, including easterly and westerly dips), combined with the possible massive nature of bedrock (in places) in the general study area (fig. 1*B*), make conventional reflection imaging less effective than refraction tomography methods in our study area (fig. 7*A*).

Combining the seismic images, we provide two alternative interpretations of the subsurface structure at Dimond Park, models 1 and 2. In model 1 (fig. 10*A*), we interpret the steeply dipping trace of the PRF (referred to herein as the main trace) to coincide with the seismically imaged anomalies between meters 150 and 160 of our seismic profile. We interpret these anomalies as representing a near-vertical (~79°) fault, with a slight reverse (up to the northeast) component (fig. 10*A*). We interpret a 40–50 m vertical offset in bedrock (Kfn in fig. 1*B*) across the fault. Based on our seismic images, our model 1 suggests the main trace of the PRF is located about 50 m farther north and strikes more northwesterly than geologically mapped at Dimond Park (fig. 11). In model 2 (fig. 10*B*), we infer two near-surface traces of the PRF, the more steeply dipping main trace shown in figure 10*A* and another lower angle (~62° NE) trace that extends further to the southwest (fig. 10*B*). In both models 1 and 2, the high-angle fault would be considered the main fault trace of the PRF at Dimond Park.

The main trace appears to extend to within a few meters of the surface, and there may be additional splays to the northeast, as indicated by vertical offsets of the 1,500 m/s velocity contour (owing to groundwater), sharp changes in the S-wave velocity, the V_P/V_S ratio and the Poisson's ratio models, and diffractions on the reflection stack. The main trace of the PRF also appears to be a groundwater barrier, and the main fault zone appears not to be water-saturated at depths above 40 m.

A better understanding of the hazards posed by the PRF is needed because of the large population that resides above and along it. If the PRF is a Holocene-active fault, surface rupture

is a clear hazard to the numerous structures along the fault. However, because the PRF separates distinctly different lithologies, strong ground shaking may also be an important hazard. We examine two possible extremes of S-wave velocity at 30 meters depth (V_{S30}) along the seismic profile (fig. 12). On the basis of refraction tomography, V_{S30} on the southwestern side of the fault (meter 75) is as low as 347 m/s, and the site would be NEHRP-classified as a "stiff soil." However, on the basis of MASW/MALW, V_{S30} on the southwestern side of the fault (meter 75) is as low as 383 m/s, which would make the site NEHRP-classified as "very dense soil/soft rock." Tomographically determined V_{S30} on the northeastern side of the fault (meter 249) is as high as 792 m/s, with MASW/MALW-determined V_{S30} as high as 767 m/s, which makes the site NEHRP-classified as "rock" (fig. 12). The NEHRP classification suggests the southwestern side of the fault has greater potential for soil amplification; however, the northeastern side of the fault also has potential for amplification because it is located on the hanging wall of a reverse fault, and it is located on a topographic high. In addition to the hazards posed by fault slip and site amplification along the PRF, its possible connection to the main trace of the Hayward Fault suggests that there is also the added hazard from fault-zone-guided waves that can travel along the PRF during a major event on the Hayward Fault.

Although it is unclear whether there are datable materials in the immediate vicinity of our seismic profile, our seismic images suggest that the PRF likely extends to depths that are shallow enough for conventional paleoseismic trenching in the active creek channel just northwest of our profile or other locations along the extent of the fault. Thus, we recommend the placement of a trench along the fault to determine its slip history.

Acknowledgments

We thank the rangers of Dimond Park for access to the park. We thank Jermile Erdem, Ryan Fay, Gini Gandhok, Adrian McEvilly, and Seth Shuler for assistance in the field. Funding was provided by the USGS Earthquake Hazards Program and the Earthquake Science Center, Menlo Park, California. We thank Andrew Meigs and Russ Graymer for critical reviews.

References Cited

Blake, M.C., Jr., Howell, D.G., and Jayko, A.S., 1984, Tectonostratigraphic terranes of the San Francisco Bay Region, *in* Blake, M.C., ed., Franciscan Geology of Northern California: Pacific Section, Society of Economic Paleontologists and Mineralogists, v. 43, p. 5–22.

Catchings, R.D., Rymer, M.J., Goldman, M.R., Sickler, R.R., and Criley, C.J., 2014, A method and example of seismically imaging near-surface fault zones in geologically complex areas using V_P, V_S, and their ratios: Bulletin of the Seismological Society of America, v. 104, p. 1989–2006, doi:10.1785/0120130294.

Graymer, R.W., 2000, Geologic map and map database of the Oakland metropolitan area, Alameda, Contra Costa, and San Francisco Counties, California: U.S. Geological Survey Miscellaneous Field Studies 2342, 31 p., 1 sheet, scale 1:50,000, 20 Arc-Info databases.

Graymer, R.W., Bryant, W., McCabe, C.A., Hecker, S., and Prentice, C.S., 2006, Map of Quaternary-active faults in the San Francisco Bay region: U.S. Geological Survey Scientific Investigations Map, 2919, 1 sheet, scale 1:275,000.

Graymer, R.W., Jones, D.L., and Brabb, E.E., 1995, Geology of the Hayward Fault zone—A digital map database: U.S. Geological Survey Open-File Report 95-597.

Hayashi, K., 2008, Development of surface-wave methods and its application to site investigations: Kyoto, Japan, Kyoto University, Ph.D. Dissertation, 315 p., http://dx.doi.org/10.14989/doctor.k13774.

Hayashi, K., and Suzuki, H., 2004, CMP cross-correlation analysis of multi-channel surface-wave data: Exploration Geophysics, v. 35 no. 1, p. 7–13.

Hole, J.A., 1992, Nonlinear high-resolution three-dimensional seismic traveltime tomography: Journal of Geophysical Research, v. 97, p. 6553–6562

Park, C.B., Miller, R.D., and Xia, J., 1999, Multichannel analysis of surface waves: Geophysics, v. 64, p. 800–808.

Trench, David, Catchings, Rufus, Buga, Michael, Pearce, J.T., Goldman, Mark, Chan, Joanne, and Criley, Coyn, 2016, Preliminary Technical Report, Collaborative Research with Fugro Consultants, Inc., and the USGS, Pilot Study—Constraining the Presence and Location of the Piedmont Thrust Splay, Oakland, CA: U.S. Geological Survey National Earthquake Hazards Reduction Program Award Number G15AP00025, 28 p.

Figures

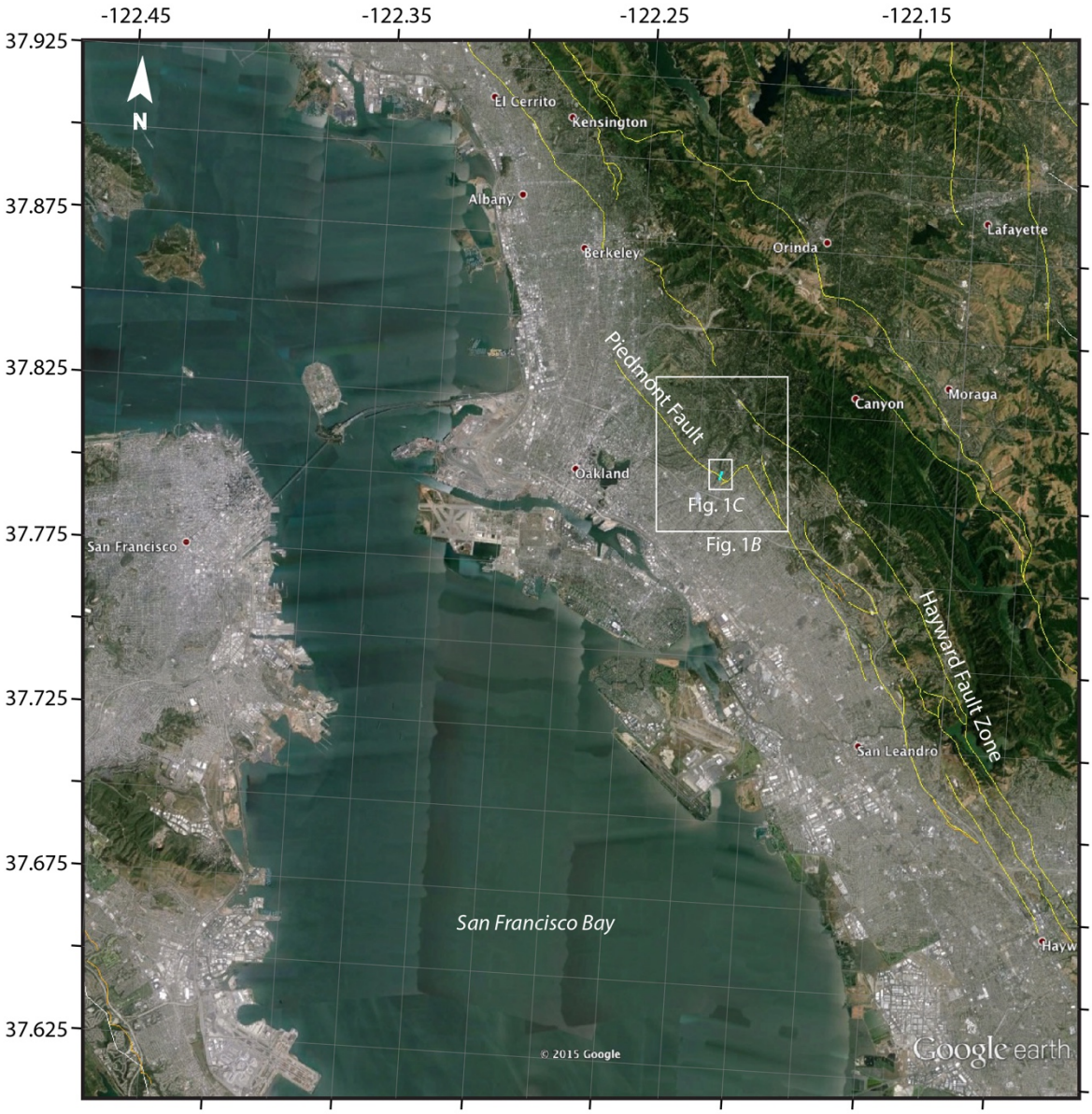

Figure 1*A*. Google Earth image of the central San Francisco Bay showing the location of the study area with respect to the Hayward Fault zone (Graymer and others, 1995). White rectangles show the approximate locations of *B* and *C*. The Dimond Park seismic profile is shown as a blue line across the Piedmont Fault.

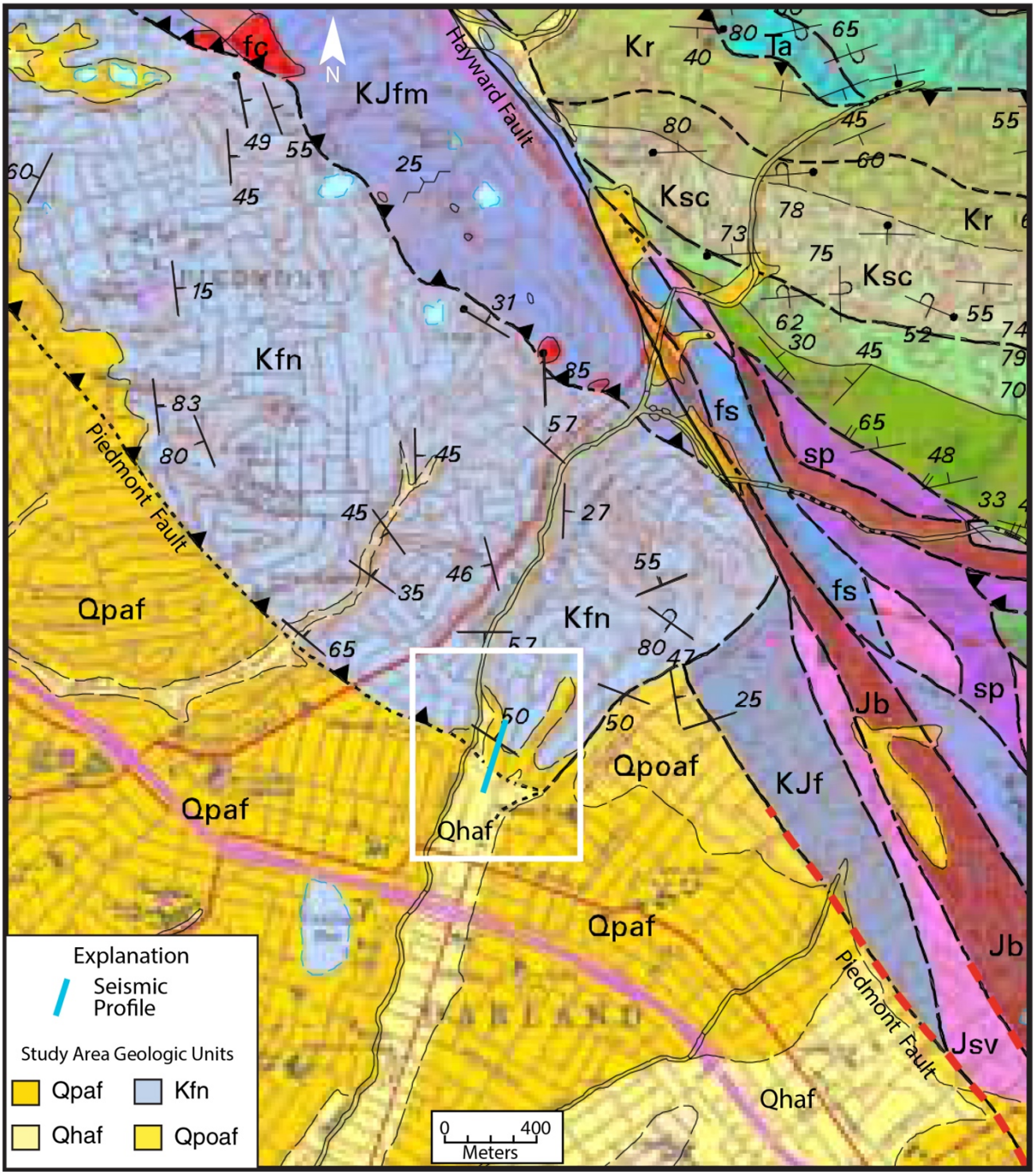

Figure 1*B*. Geologic map of the study area (from Graymer, 2000) showing geologic units and stratigraphic strikes and dips. Units in the study area are as follows: Kfn—Sandstone of the Novato Quarry terrane of Blake and others (1984); Qpoaf—Pleistocene older alluvial fan deposits; Qpaf—Pleistocene alluvial fan and fluvial deposits; Qhaf—Holocene alluvial fan and fluvial deposits. See Graymer (2000) for description of map units and definition of other units shown. Seismic profile is shown as the cyan-colored line. White rectangle shows location of *C*.

Figure 1*C*. Google Earth image showing a close up of the Dimond Park seismic profile (blue line) relative to the Piedmont Fault (yellow lines).

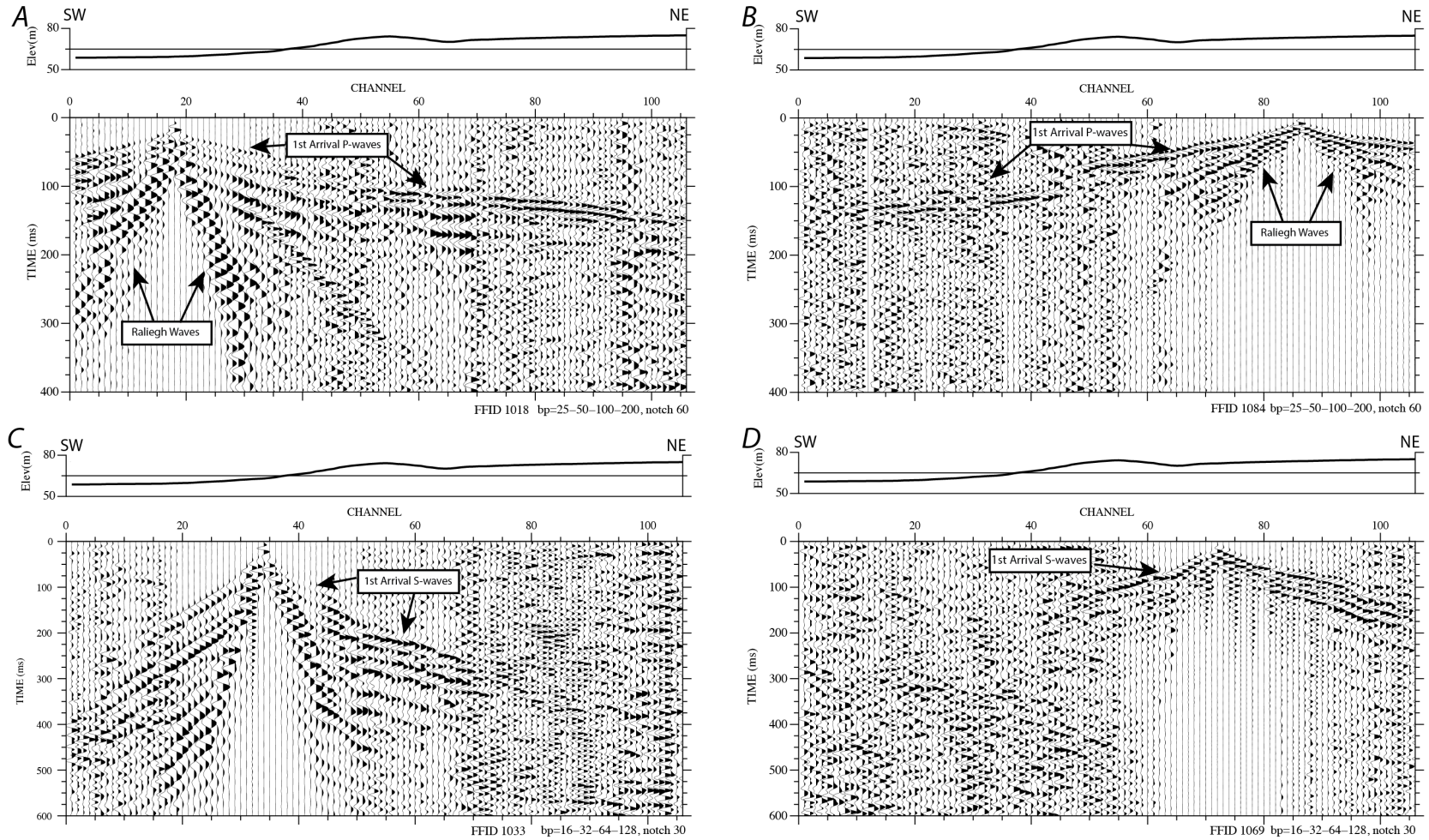

Figure 1. Seismic reflection images showing example shot gathers from the Dimond Park seismic profile with the topographic profile above each shot gather. Lower graphs show 400 (*A*,*B*) and 600 (*C*,*D*) milliseconds (ms) of seismic data acquired at each geophone. *A*, Example P-wave shot gather from a shot point located near the southwestern end of the Dimond Park seismic profile. *B*, Example P-wave shot gather from a shot point located near the northeastern end of the Dimond Park seismic profile. *C*, Example S-wave shot gather from a shot point located near the southwestern end of the Dimond Park seismic profile. *D*, Example S-wave shot gather from a shot point located near the northeastern end of the Dimond Park seismic profile.

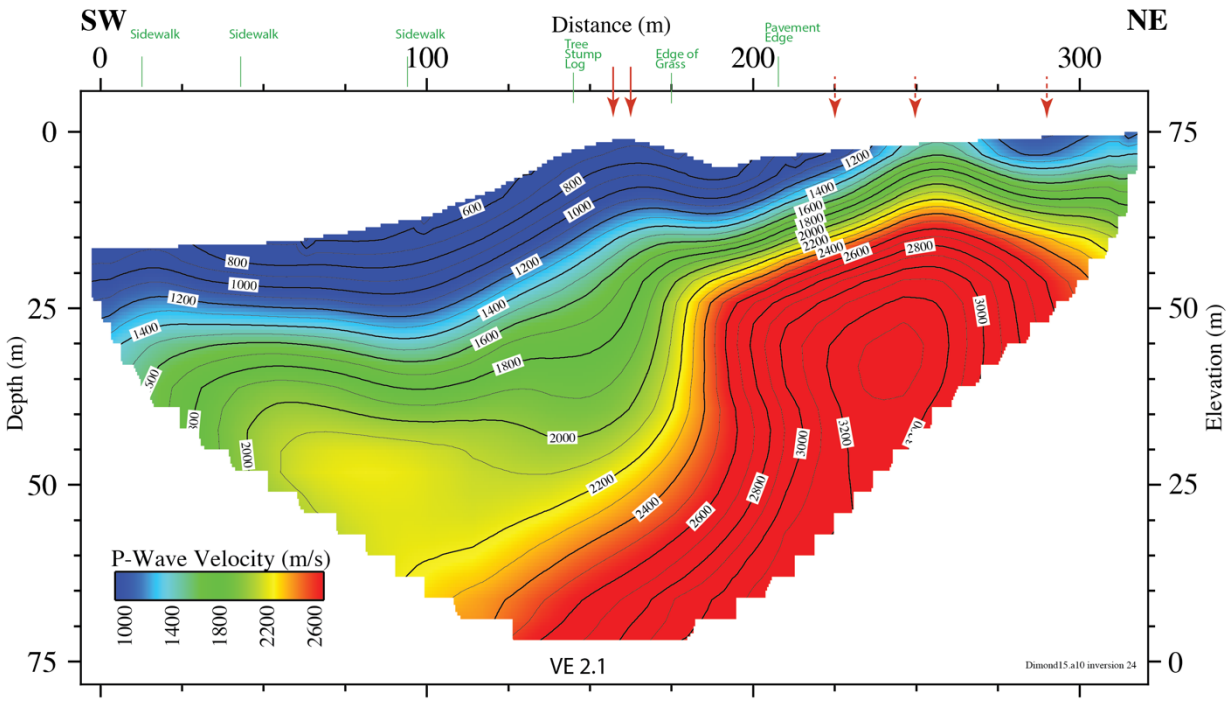

Figure 2. Model of P-wave refraction tomography velocity along the Dimond Park seismic profile. Depth (left side) is relative to the topographically highest point along the seismic profile. Elevation (right side) is relative to sea level. Landmarks along the seismic profile are shown in green. Solid vertical red arrows mark the location of the Piedmont Reverse Fault zone and dashed red arrows mark locations of other possible near-surface faults. The 1,500 m/s contour is shown in white.

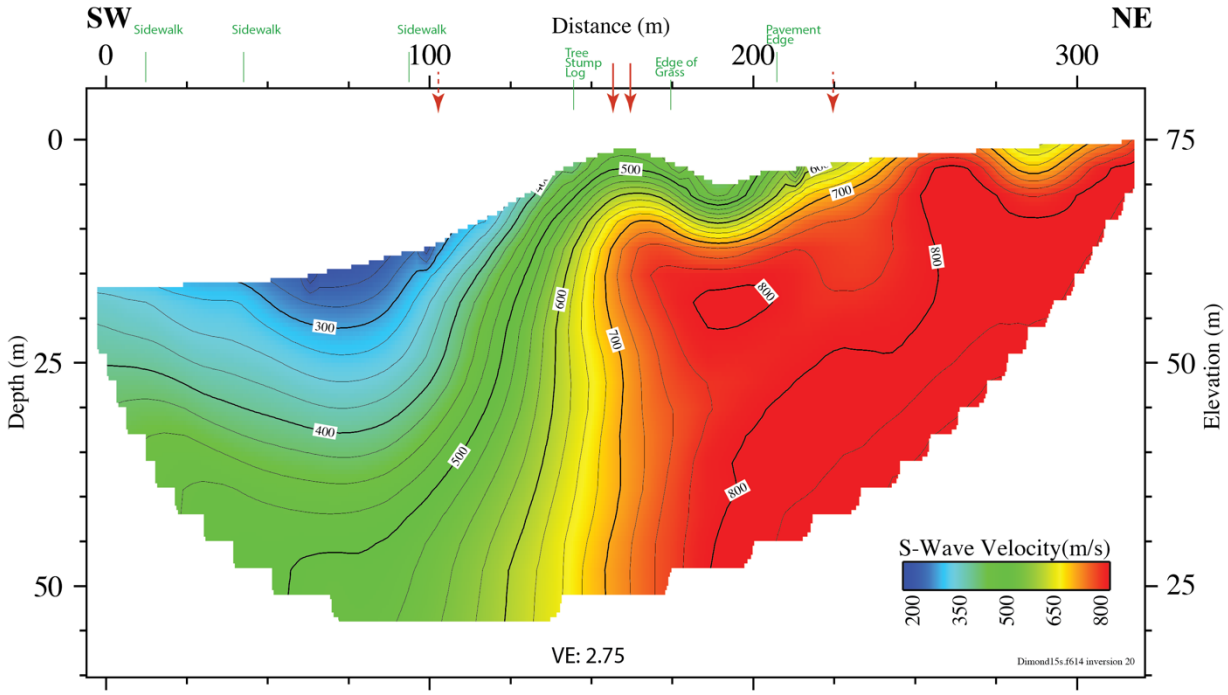

Figure 3. Model of S-wave refraction tomography velocity along the Dimond Park seismic profile. Depth (left side) is relative to the topographically highest point along the seismic profile. Elevation (right side) is relative to sea level. Landmarks along the seismic profile are shown in green. Solid vertical red arrows mark the location of the Piedmont Reverse Fault zone and dashed red arrows mark locations of other possible near-surface faults.

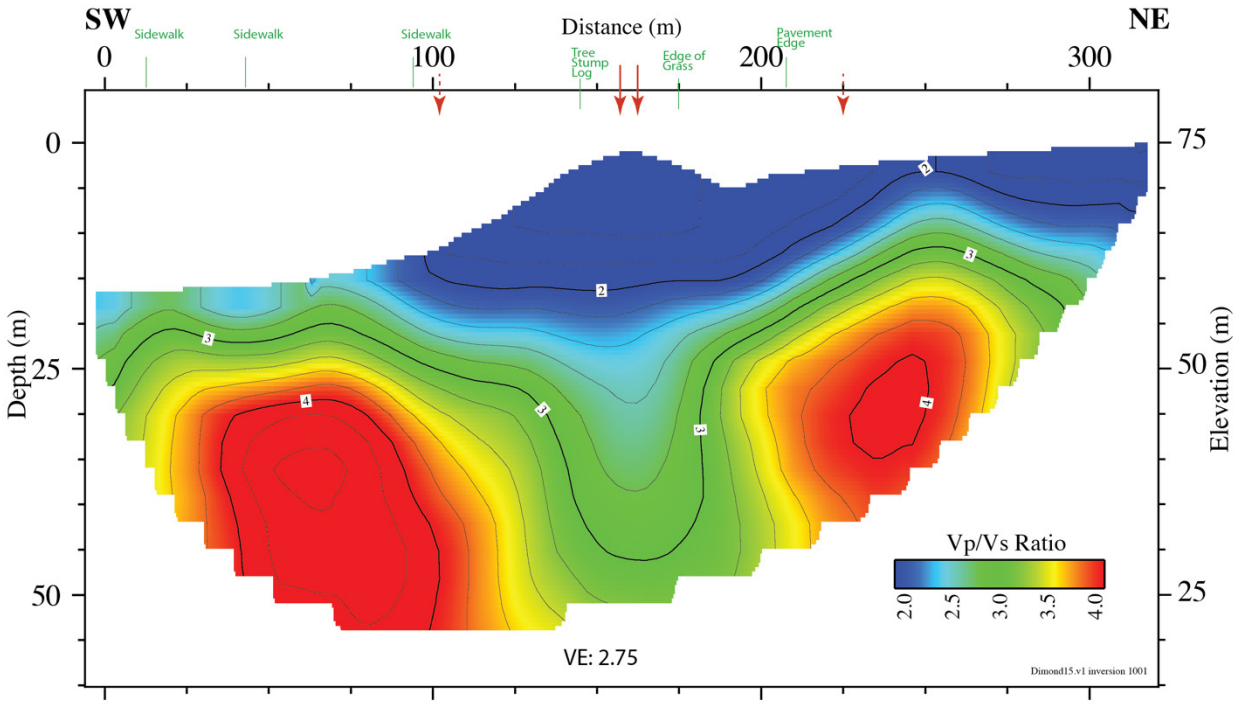

Figure 4. Model of V_P/V_S (P-wave velocity to S-wave velocity) ratio along the Dimond Park seismic profile. Depth (left side) is relative to the topographically highest point along the seismic profile. Elevation (right side) is relative to sea level. Landmarks along the seismic profile are shown in green. Solid vertical red arrows mark the location of the Piedmont Reverse Fault zone and dashed red arrows mark locations of other possible near-surface faults.

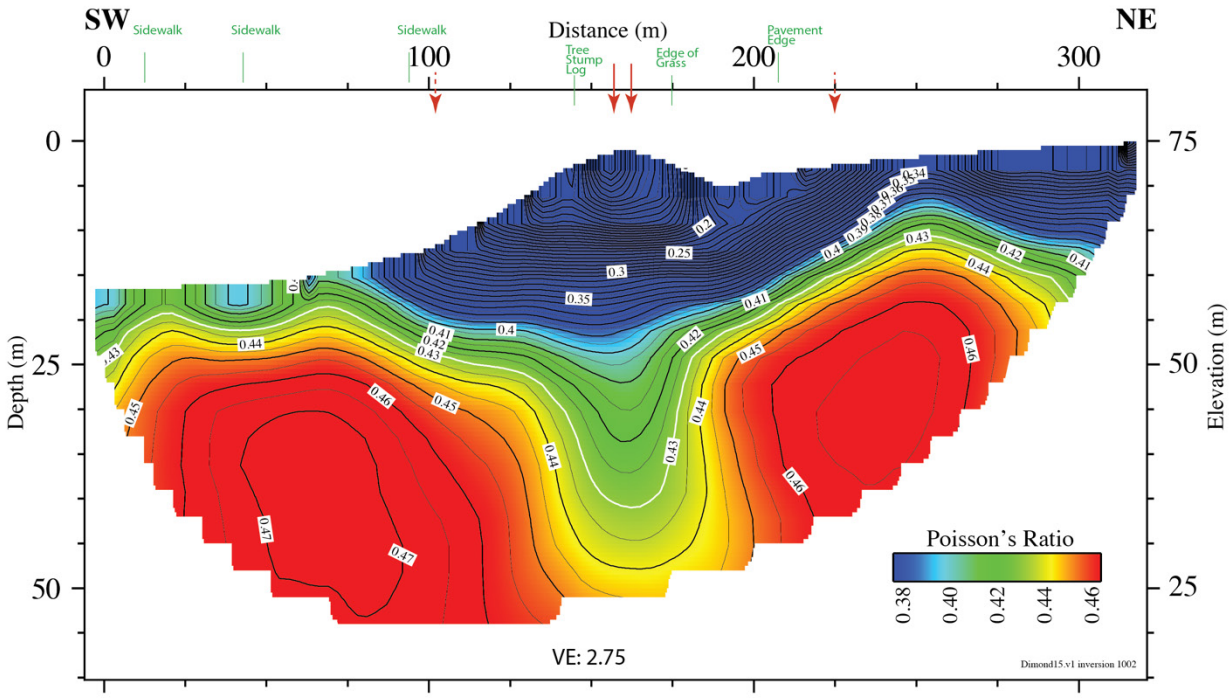

Figure 5. Model of Poisson's ratio along the Dimond Park seismic profile. Depth (left side) is relative to the topographically highest point along the seismic profile. Elevation (right side) is relative to sea level. Landmarks along the seismic profile are shown in green. Solid vertical red arrows mark the location of the Piedmont Reverse Fault zone, and dashed red arrows mark the locations of other possible near-surface faults. The 0.43 contour is shown in white.

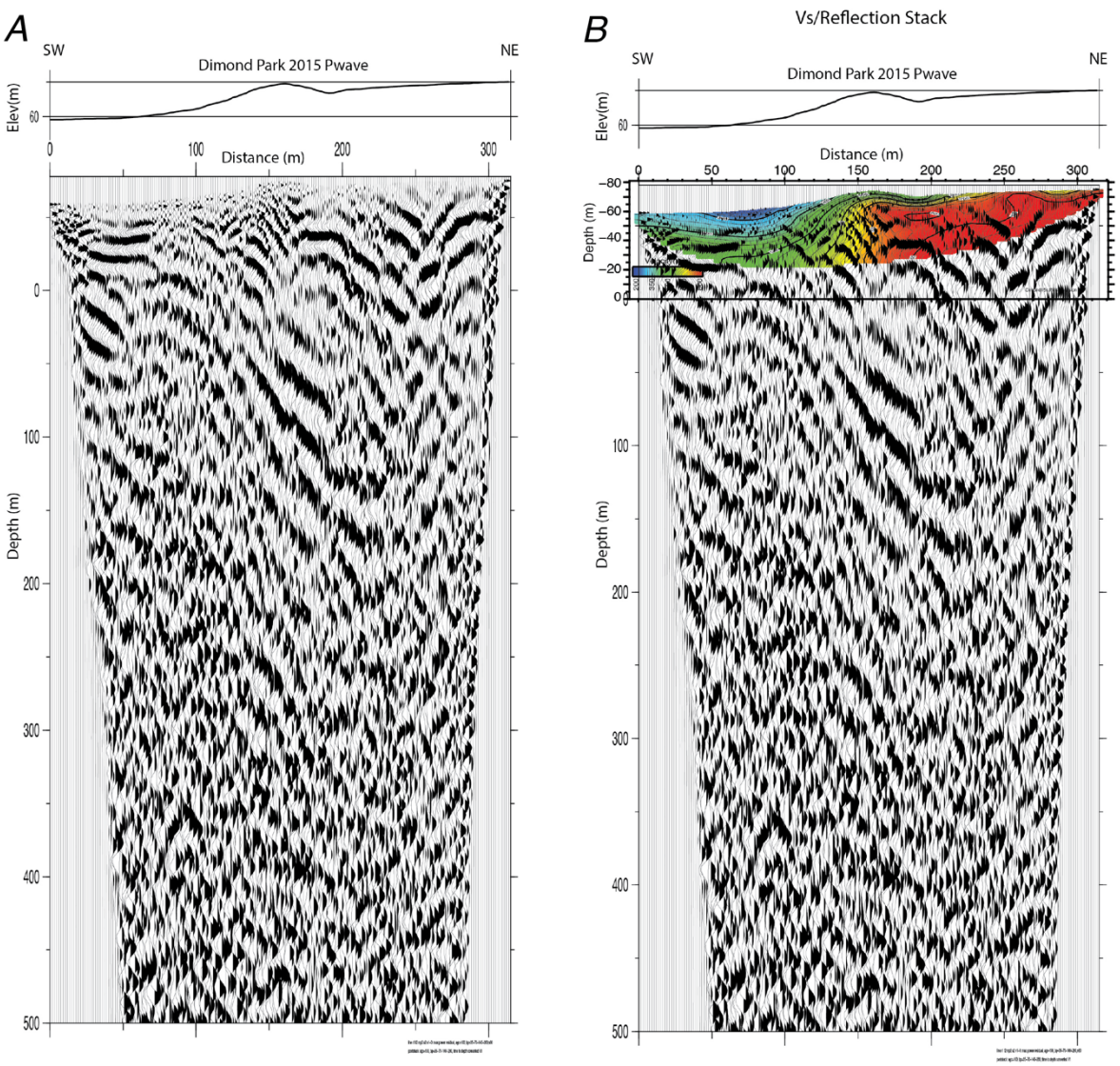

Figure 6. Stacked reflection images along the Dimond Park seismic profile. Depth is relative to sea level. In *B*, stacked reflection image from *A* is superimposed on the S-wave tomographic velocity model from figure 4.

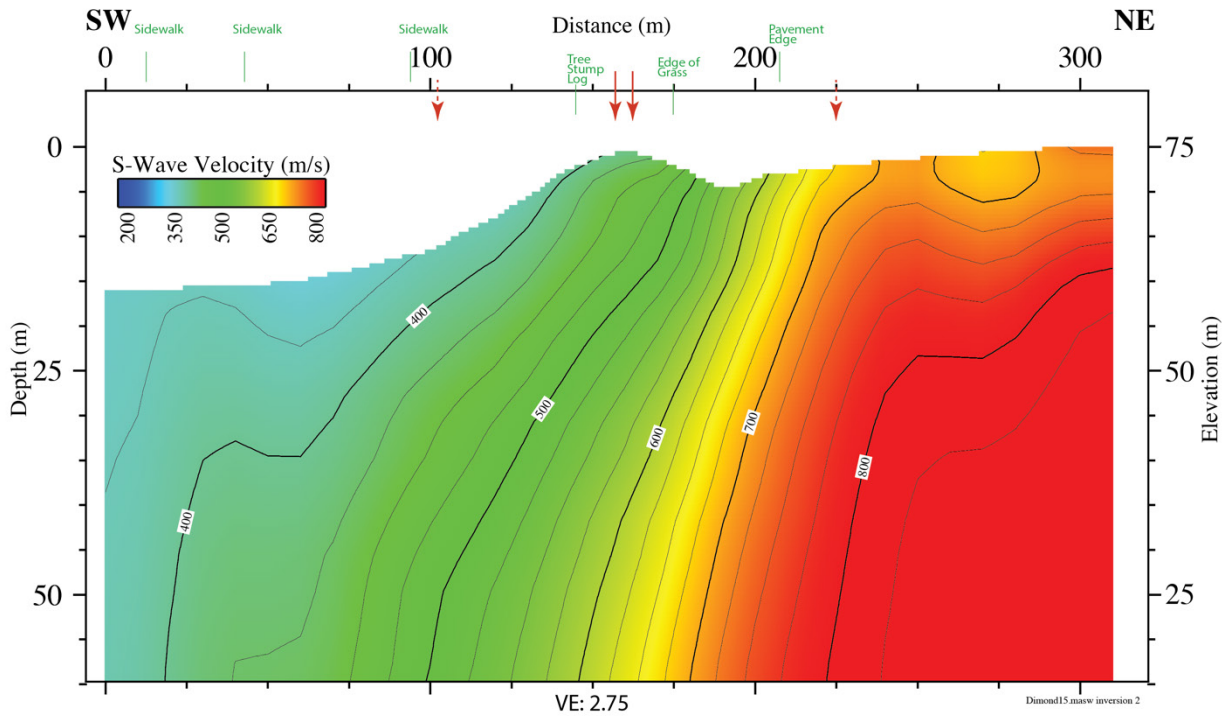

Figure 7. Model of S-wave velocity along the Dimond Park seismic profile determined using the Multi-channel Analysis of Surface Waves (MASW) method and Raleigh waves from our P-wave data. Depth (left side) is relative to the topographically highest point along the seismic profile. Elevation (right side) is relative to sea level. Landmarks along the seismic profile are shown in green. Solid vertical red arrows mark the location of the Piedmont Reverse Fault zone and dashed red arrows mark locations of other possible near-surface faults.

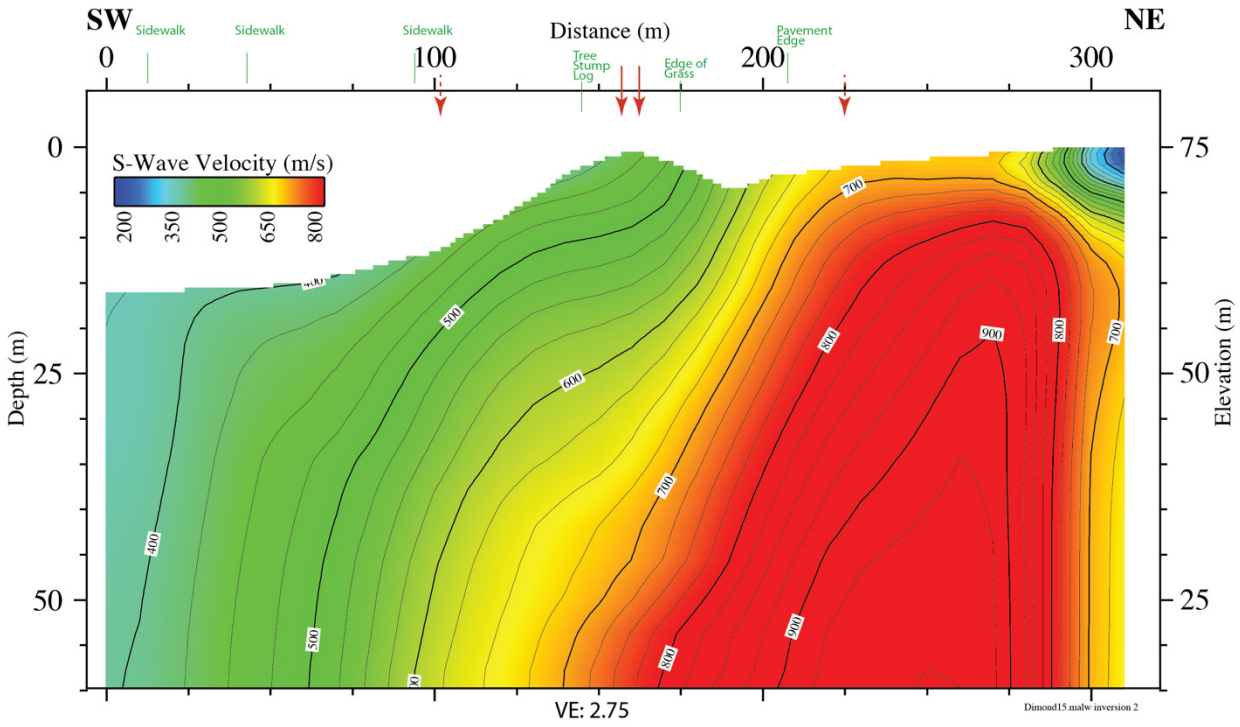

Figure 8. Model of S-wave velocity along the Dimond Park seismic profile determined using the MALW method and Love waves from our S-wave data. Depth (left side) is relative to the topographically highest point along the seismic profile. Elevation (right side) is relative to sea level. Landmarks along the seismic profile are shown in green. Solid vertical red arrows mark the location of the Piedmont Reverse Fault zone and dashed red arrows mark locations of other possible near-surface faults.

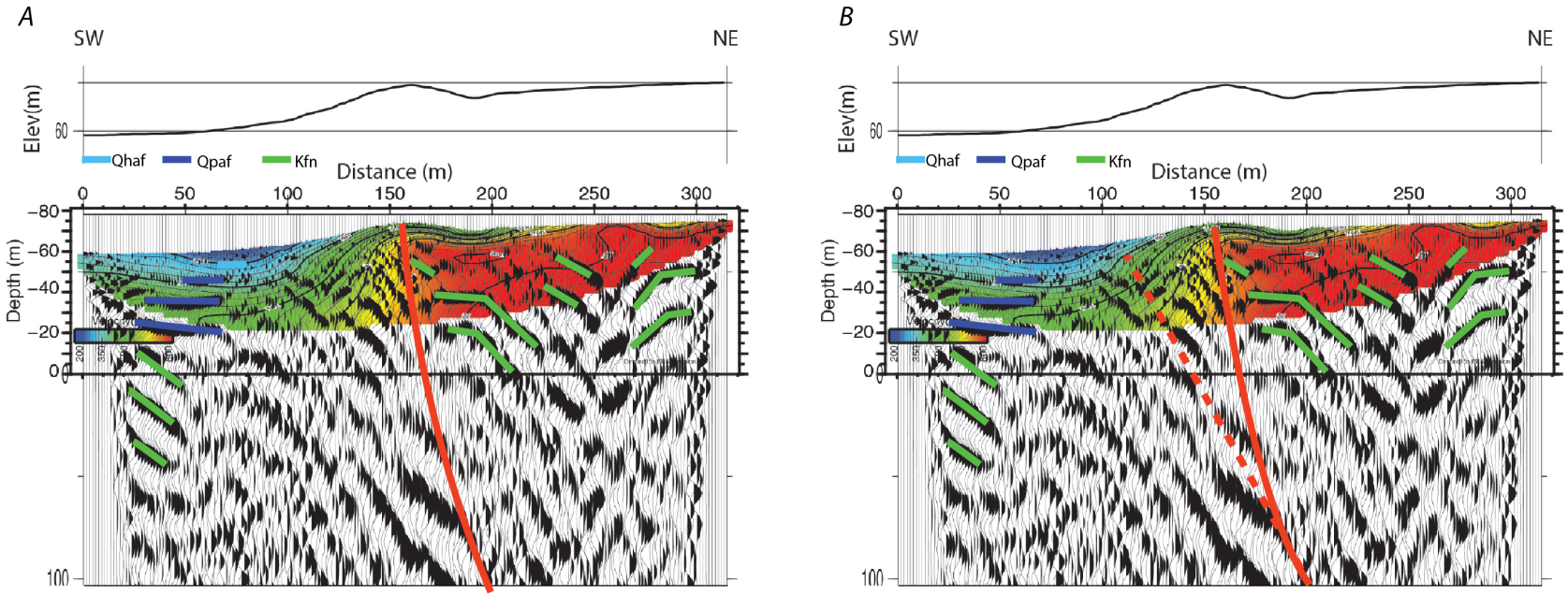

Figure 9. Expanded view of the upper 100 m of the stacked reflection images (from fig. 7) with the superimposed S-wave velocity model (from fig. 4) and geologic interpretation from model 1 (*A*) and model 2 (*B*). The red lines shows interpreted main trace of the Piedmont Reverse Fault. Geologic units are shown and described in figure 1*B*.

Figure 10. Google Earth image of study area from figure 1*C*, with faults (solid yellow lines) from Graymer and others (2006), interpreted fault location on the basis of seismic images (dashed line), and seismic profile location (cyan line). Note that the previous fault mapping is plotted at scale well beyond its intended scale, suggesting a level of precision not present in the original work.

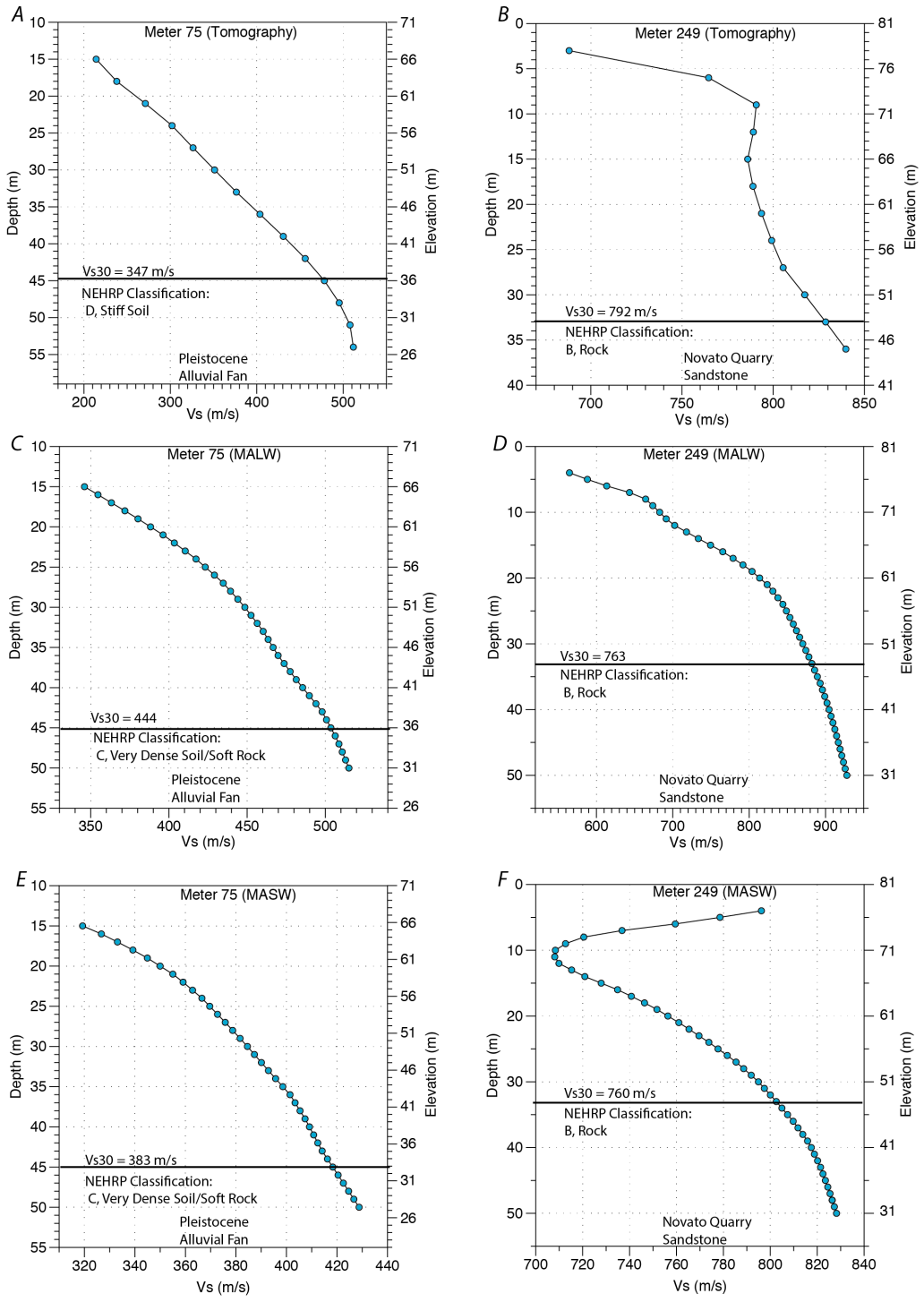

Figure 11. Plots of one-dimensional velocity-depth functions (S-wave) and National Earthquake Hazards Reduction Program (NEHRP) classifications at discrete locations along the Dimond Park seismic profile. *A*, Tomographic velocities at meter 75. *B*, Tomographic velocities at meter 249. *C*, Multi-channel Analysis of Love Waves (MALW) velocities at meter 75. *D*, MALW velocities at meter 249. *E*, Multi-channel Analysis of Surface Waves (MASW) velocities at meter 75. *F*, MASW velocities at meter 249. Depth (left side) is relative to the topographically highest point along the seismic profile. Elevation (right side) is relative to sea level.

https://dx.doi.org/10.3133/
ofr 20161123